Uncertainty analysis of microscopic parameters obtained from the single parabolic band modeling of thermoelectric materials

H. Naithani,[1,*] E. Müller,[1,2] and J. de Boor[1,3,†]

[1] *Institute for Frontier Materials on Earth and in Space, German Aerospace Center (DLR), Cologne, Germany*
[2] *Institute of Inorganic and Analytical Chemistry, Justus Liebig University of Giessen, Giessen, Germany*
[3] *Institute of Technology for Nanostructures (NST) and CENIDE, University of Duisburg-Essen, Duisburg, Germany*

(Received 1 April 2025; revised 25 July 2025; accepted 9 September 2025; published 28 October 2025)

The single parabolic band (SPB) model is a popular, easy-to-use, and somewhat powerful tool to describe thermoelectric transport and is often employed for material optimization and the extraction of band structure parameters. While the fundamental limitations of the model are well-known and usually recognized, a discussion on the uncertainty in the derived parameters when the model is valid is missing, but indispensable for a qualified comparison and analysis of reported values. In this work, we derive analytical expressions for the uncertainty in the modeling parameters—the reduced Fermi level, density of states (DOS) mass, carrier concentration (n), mobility parameter (μ_0), Lorenz number (L), and electronic thermal conductivity (K_E) based on experimental uncertainty in the Seebeck coefficient (α), electrical conductivity (σ), and Hall coefficient (R_H). As the uncertainty in the SPB-derived quantities resulting from the Seebeck coefficient depends not only on the uncertainty of the Seebeck coefficient but also on the Seebeck coefficient value itself, it is discussed in detail. The uncertainty in the most cited parameter derived from the SPB model, i.e., the DOS mass, is dominated by the uncertainty arising due to α. For a relative uncertainty of 5% in α alone, the uncertainty in the DOS mass ranges from 5% to 15% for 50–400 μV/K, whether scattering of electrons by acoustic phonons, polar optical phonons, ionized impurities, or neutral impurities is assumed. Associated challenges to accurate and insightful modeling of the thermoelectric (TE) materials are discussed and exemplified by an analysis of DOS masses for Mg_2Si from various literature sources, where the observed large scatter can be rationalized by large but realistic uncertainties in α and R_H, thereby highlighting the need for better measurement protocols.

DOI: 10.1103/lqtf-rvlm

I. INTRODUCTION

Thermoelectric (TE) materials utilize temperature differences to generate electricity and vice versa. Generators from these materials are solid-state devices that last long, are highly reliable, and require virtually no maintenance. This has prompted their extensive usage in powering space missions, with the first spacecraft using a radioisotope TE generator being launched in 1961 [1,2]. Among terrestrial applications, TE materials have found commercial success as the key components in portable coolers [3] and are being researched for prospective utilization of waste heat from industries [4]. TE generators suffer from lower heat-to-power conversion efficiency than their traditional counterparts such as turbine-based generators, which prevents their widespread use. Thus, increasing the performance of TE materials is the focal point of current TE research.

The performance of a TE material is determined by the figure of merit, $zT = (\alpha^2\sigma/\kappa)T$, with a higher value corresponding to a higher efficiency. Here, α denotes the Seebeck coefficient, σ and κ denote electrical and thermal conductivity, respectively, and T denotes temperature. Efforts aiming at the synthesis of high zT materials are complemented and guided by attempts to understand the underlying electronic band structures of such materials [5–7]. Certain parameters associated with the electronic band structure of a material, such as the density of states (DOS), mass, m^*_D, the deformation potential, E_{def}, the band gap, E_g, etc., aid in predicting TE properties and, in turn, zT. More importantly, knowledge of these parameters provides quantifiable metrics to further improve existing TE materials and discover promising new ones. The simplest way to model the electronic band structure of a

*Contact author: Harshita.Naithani@dlr.de
†Contact author: Johannes.deBoor@dlr.de

material assumes that a single parabolic band (SPB) is sufficient to describe the electronic behavior of a TE material, usually assumed to be rigid, i.e., independent of temperature or dopant concentration. At high carrier concentrations (typical of most high-performance TE materials) and at temperatures below the maximum zT, minority carrier effects are negligible and the SPB model appears to be valid. The SPB assumption leads to simple equations for the measurable thermoelectric transport properties, which can be solved numerically to obtain material parameters such as the DOS mass, mobility parameter (μ_0), and lattice thermal conductivity (κ_L) [8]. Additionally, the maximum value of zT for a material and the corresponding carrier concentration (n_{opt}) can also be predicted, thus providing easy guidance for further experimental efforts. The SPB is also employed to calculate the β parameter [8], given by $\beta = (\mu_0(m_D^*/m_e)^{3/2}T^{5/2})/\kappa_L$ (here, m_e denotes the rest mass of an electron), which determines the optimal performance of TE materials and is, therefore, an easy but more convincing metric than zT for the evaluation and comparison of novel TE materials. In more complex cases, estimation of the effective SPB parameters aids in band structure engineering (e.g., band convergence [9], formation of resonant states [10]) or isovalent doping/solid solution formation [11] and is, thus, crucial for fast material optimization. However, the most powerful demonstrated use of the very simple SPB modeling has been in confirming predicted band structure modifications, such as in Mg_2Si_{1-x}, Sn_x [9], where the highest apparent DOS mass for $x = 0.7$ confirmed band convergence for this particular composition. Even when the SPB model is not applicable, it can provide critical information about the electronic band structure, e.g., for $CaZn_2Sb_2$-$CaMg_2Sb_2$, where an abrupt change in the apparent DOS mass provides experimental evidence of valence band crossing [12]. The material parameters obtained using the SPB model can be compared with those obtained from first-principles methods to check for inconsistencies and generate confidence in our understanding of material properties. Moreover, when more advanced models (like two- or three-band models) are required to model the data, pertinence of the SPB model is preserved as it provides starting points and consistency checks for these models [13,14]. These advantages have prompted a large number of TE researchers, particularly experimentalists, to adopt SPB modeling to varying degrees in their research [9,10,15–25].

The SPB model is inapplicable when the conducting band is nonparabolic or when more than one band participates in carrier transport [13,26–29]. For materials with these features, the SPB model cannot predict the maximum zT. Even in materials for which the transport properties can be described with two degenerate bands, where the SPB model has been shown to be applicable, the carrier concentration cannot be predicted accurately, which limits its utility in further analysis of the material properties [30]. Moreover, it has been observed that good thermoelectric materials have complex band structures [31–34] and, therefore, the SPB model can provide only limited insights into most materials of interest. While these limitations of the SPB model are well-known and documented [31], the uncertainty arising from the experimental data, i.e., – α, σ, κ, and Hall coefficient (R_H), used to obtain microscopic parameters from the SPB model is, generally, ignored. The uncertainty in measurement of the TE properties often varies with temperature [35] and from instrument to instrument. While several reports indicate that the uncertainty in the Seebeck coefficient is around 3%–5% [36–41], Mackey *et al.* [42] estimated that this uncertainty could be as high as 13% at ∼1300 K using a finite element analysis. The uncertainty in electrical conductivity is reported to be between 3% and 7% [37,41,42]. The reported uncertainty in the Hall coefficient varies from ∼5% to ∼10% [43–46]. Round-robin tests for thermal conductivity indicate that the uncertainty ranges from ∼3% to ∼9% between 300 and 800 K [38,47]. Certainly, the experimental uncertainty is not negligible. As discussed, changes in SPB-derived quantities are often employed to identify or confirm characteristics of the transport or the electronic band structure model that go beyond a simple rigid SPB model, e.g., nonrigidity, nonparabolicity of the band structure [26,31,48], multiple contributing parabolic bands [30,49,50], etc. In such cases, the SPB-derived quantities can still provide clues about the band structure of the material, e.g., the observed variation of the DOS mass with varying carrier concentration can be used to identify or confirm such phenomena. However, such changes in the SPB-derived quantities can only be used for physical interpretation if the uncertainty in the SPB parameters is smaller than the effect of changes in the electronic band structure. Among all the parameters obtained using the SPB model, the DOS mass is the one that is related closest to the chemical composition of the material and least to the microstructure (i.e., grain size, phase constitution, and grain boundary type) and, hence, to synthesis routes with details that vary from lab to lab. It is, therefore, in principle most suitable for interlab comparisons, in contrast, e.g., to the scattering potentials and lattice thermal conductivity, which are very sensitive to the microstructure. However, a large scatter is commonly observed while comparing reported DOS mass values for a given TE material, making it difficult for researchers to validate their own findings by means of comparison. Therefore, it is crucial to estimate the fraction of the scatter that can be expected from experimental uncertainty.

There is limited literature available on the propagation of uncertainty of experimental data in the SPB-derived quantities. Crawford *et al.* [51] discuss the impact of systematic error on the SPB-derived quantities with a hypothetical example, when the measurement of the Nernst coefficient is also available. To the best of our knowledge,

a generalized discussion on the propagation of uncertainty of the experimental data into band structure modeling parameters is missing. Therefore, in this work, we present a systematic study of the uncertainty in the SPB-derived quantities arising from the uncertainty, in the form of standard deviations, in the experimental quantities, i.e., α, σ, and R_{H}. Additionally, a curve fitting for relevant SPB parameters is employed to enable researchers to quickly evaluate the associated uncertainty based on their own estimate of measurement uncertainty. Interestingly, the most widely used SPB-derived parameter, i.e., the DOS mass, is determined to have a very high uncertainty. Finally, as an example, the discrepancies in the values of the DOS mass for Mg_2Si from 19 literature sources have been analyzed. It has been found that ~16% uncertainty in both the Seebeck and Hall coefficients can account for the observed scatter in the DOS mass values, highlighting the need for improved measurement protocols.

II. Theory

For most of the heavily doped TE materials, the minority carriers have a negligible effect on the TE properties, namely α, σ, R_{H}, and κ, for a wide range of temperatures. For such materials, a single parabolic band description is assumed to be sufficient to model these properties. A detailed discussion on the SPB model itself, with its merits and shortcomings, can be found elsewhere [8,30,49]. When the SPB model is used to derive band structure parameters, the uncertainty in the experimental data (here, α, σ, and R_{H}) propagates into these derived quantities. Measurement uncertainty is quantified in terms of the standard deviation, *SD*, of the measurement, i.e., a measure of variability in the measured data, which is defined as $SD = \sqrt{(1/n-1)\sum_{k=1}^{n}(q_k-\bar{q})^2}$, where q_k is the kth measurement and $\bar{q}$ is the mean of the measurand. The general formula for estimating *SD* of a quantity A, which is a function of $x_1, \ldots, x_n$, in terms of the *SD*s in each of $x_1, \ldots, x_n$, is given by [52]

$$SD_A^2 = SD_{x_1}^2\left(\frac{\partial A}{\partial x_1}\right)^2 + SD_{x_2}^2\left(\frac{\partial A}{\partial x_2}\right)^2 + \ldots + SD_{x_n}^2\left(\frac{\partial A}{\partial x_n}\right)^2. \quad (1)$$

The SPB model is derived from the Boltzmann transport equation, where an applied force shifts the carriers away from equilibrium and collisions tend to bring the carriers to equilibrium. Thus, carrier transport is governed by the scattering mechanisms that, for simplicity, are characterized by a carrier relaxation time [53]. The SPB equations provided here assume a power law form of the relaxation time, τ, given by $\tau = \tau_0\epsilon^{\lambda-0.5}$, where λ is called the scattering parameter with its value depending upon the scattering mechanism and ϵ is the carrier energy E in reduced units, i.e., $\epsilon = E/k_{\mathrm{B}}T$, where k_{B} and T denote the Boltzmann constant and temperature, respectively. Next, we use the following form of the Fermi-Dirac integrals:

$$\mathcal{F}_j \equiv \mathcal{F}_j(\eta) = \frac{1}{\Gamma(j+1)}\int_0^\infty \frac{\varepsilon^j\, d\varepsilon}{1+\exp(\varepsilon-\eta)} \quad \text{for } j > -1, \quad (2)$$

where Γ denotes the gamma function and $\mathcal{F}_j$ relates to a slightly different form of the Fermi-Dirac integral, F_j, which is commonly used in the SPB equations. This is given by

$$F_j(\eta) = \int_0^\infty \frac{\varepsilon^j\, d\varepsilon}{1+\exp(\varepsilon-\eta)} = \Gamma(j+1)\mathcal{F}_j(\eta) \text{ for } j > -1. \quad (3)$$

It is advantageous to use Eq. (2) since, unlike Eq. (3), it is defined for negative integers using the identity $\mathcal{F}_{j-1} = d\mathcal{F}_j/d\eta$ [54]. This property is used when deriving the expressions for computing *SD*s using Eq. (1). The analytical expressions are derived assuming that λ is known. The relevant SPB equations [8] using $\mathcal{F}_j$, along with the expressions for the respective *SD* [derived from Eq. (1)] in the SPB model-derived quantities, are listed below.

1. The reduced Fermi level (η) is determined first, using the expression for the Seebeck coefficient

$$\alpha = \left(\frac{k_b}{q}\right)\left(\frac{(2+\lambda)\Gamma(\lambda+2)\mathcal{F}_{\lambda+1}}{(1+\lambda)\Gamma(\lambda+1)\mathcal{F}_\lambda} - \eta\right). \quad (4)$$

As η depends only on the Seebeck coefficient, *SD* in η is given by

$$SD_\eta^2 = SD_\alpha^2\left(\frac{\partial\eta}{\partial\alpha}\right)^2. \quad (5)$$

Since Eq. (4) is an invertible function, $\partial\eta/\partial\alpha$ can be expressed analytically using the expression

$$\frac{\partial\eta}{\partial\alpha} = \frac{1}{\partial\alpha/\partial\eta}.$$

The reduced Fermi level, η, for typically good TE materials, takes values close to zero, making the relative *SD* in η very large and meaningless. However, in most other cases, it is more convenient and practical to use relative standard deviation (hereon denoted by *sd*). For all other SPB model-derived quantities, *sd*s, denoted by sd_A where $sd_A = SD_A/A$ are used, where A denotes the absolute value of the physical quantity for which the relative standard deviation is being calculated.

2. The value of η is then used to calculate the Hall prefactor, r_{H}, as

$$r_{\mathrm{H}} = \frac{3\sqrt{\pi}}{4}\frac{\mathcal{F}_{0.5}(\eta)(0.5+2\lambda)\Gamma(0.5+2\lambda)\mathcal{F}_{(2\lambda-0.5)}}{(1+\lambda)^2(\Gamma(1+\lambda))^2{\mathcal{F}_\lambda}^2}. \quad (6)$$

Using the Hall prefactor and the Hall coefficient (R_{H}), the carrier concentration, n, can be calculated as follows:

$$n = r_{\mathrm{H}}/eR_{\mathrm{H}}. \quad (7)$$

The relative standard deviation in the carrier concentration, sd_n, is given by

$${sd_n}^2 = {sd_{R_{\mathrm{H}}}}^2 + \left(\frac{SD_\alpha}{r_{\mathrm{H}}}\right)^2\left(\frac{\partial r_{\mathrm{H}}}{\partial\eta}\right)^2\left(\frac{\partial\eta}{\partial\alpha}\right)^2. \quad (8)$$

3. The DOS mass, ${m^*}_D$, can be calculated from the expression for the carrier concentration

$$n = 2\left(\frac{2\pi {m^*}_D k_{\mathrm{B}} T}{h^2}\right)^{3/2}\mathcal{F}_{1/2}. \quad (9)$$

Here, k_{B}, e, and h denote the Boltzmann constant, elementary charge, and Planck's constant, respectively. Using Eqs. (6), (7), and (9), the DOS mass can be expressed as follows:

$$m_D^* = K\left(\frac{1}{R_H}\right)^{2/3} J_{m_D^*}. \quad (10)$$

Here,

$$K = \frac{h^2}{2\pi m_e k_B T}\left(\frac{3\sqrt{\pi}}{8e}\right)^{2/3}$$

summarizes the quantities that do not depend on η and

$$J_{m_D^*} = \left(\frac{(0.5+2\lambda)\Gamma(0.5+2\lambda)}{(1+\lambda)^2(\Gamma(1+\lambda))^2}\frac{\mathcal{F}_{2\lambda-0.5}}{{\mathcal{F}_\lambda}^2}\right)^{2/3}$$

summarizes the Fermi integrals. The relative standard deviation in the DOS mass, $sd_{m_D^*}$, is then given by

$${sd_{m_D^*}}^2 = \left(\frac{2}{3}sd_{R_H}\right)^2 + \left(\frac{SD_\alpha}{J_{m_D^*}}\right)^2\left(\frac{\partial\eta}{\partial\alpha}\right)^2\left(\frac{\partial J_{m_D^*}}{\partial\eta}\right)^2. \quad (11)$$

4. The electrical conductivity can be expressed as $\sigma = n_{\mathrm{H}} e \mu_{\mathrm{H}}$, where μ_{H} is the Hall mobility. As μ_{H} depends upon the Fermi level, which in turn depends upon the carrier concentration or doping, it is often desirable to work with the mobility parameter (μ_0), which is an intrinsic material parameter. Using σ, R_{H}, and η, the mobility parameter can be determined. The expression for σ is as follows [13]:

$$\sigma = \frac{\mu_0}{R_{\mathrm{H}}}\frac{(0.5+2\lambda)\Gamma(0.5+2\lambda)}{(1+\lambda)\Gamma(1+\lambda)}\frac{\mathcal{F}_{2\lambda-0.5}}{\mathcal{F}_\lambda}. \quad (12)$$

Using Eqs. (6), (7), and (12), μ_0 can be expressed as

$$\mu_0 = \frac{2}{\sqrt{\pi}}\sigma R_{\mathrm{H}} J_{\mu_0}. \quad (13)$$

Here,

$$J_{\mu_0} = \frac{(1+\lambda)\Gamma(1+\lambda)}{(0.5+2\lambda)\Gamma(0.5+2\lambda)}\frac{\mathcal{F}_\lambda}{\mathcal{F}_{2\lambda-0.5}}.$$

The relative SD in the mobility parameter, sd_{μ_0}, is given by

$${sd_{\mu_0}}^2 = {sd_\sigma}^2 + {sd_{R_{\mathrm{H}}}}^2 + \left(\frac{SD_\alpha}{J_{\mu_0}}\right)^2\left(\frac{\partial\eta}{\partial\alpha}\right)^2\left(\frac{\partial J_{\mu_0}}{\partial\eta}\right)^2. \quad (14)$$

Acoustic phonon scattering is the most commonly employed scattering mechanism when modeling thermoelectric transport properties and the associated mobility parameter relates to the deformation potential, E_{def}, by the relation

$$\mu_{0,\mathrm{AP}} = \frac{\pi\sqrt{8}\hbar^4 e\rho {v_{\mathrm{l}}}^2 {N_{\mathrm{v}}}^{5/3}}{4E_{\mathrm{def}}^2 {m^*}_D{}^{2.5}(k_{\mathrm{B}}T)^{3/2}}, \quad (15)$$

where ρ, v_{l}, and N_{v} denote material density, longitudinal velocity of sound in the material, and the degeneracy of the electronic band, respectively. Additionally, $sd_{E_{\mathrm{def}}}$ can then be evaluated as

$${sd_{E_{\mathrm{def}}}}^2 = \left(\frac{1}{2}sd_{\mu_0}\right)^2 + \left(\frac{5}{4}sd_{{m^*}_D}\right)^2. \quad (16)$$

5. The Lorenz number (L) is used to evaluate the electronic thermal conductivity. It is given by

$$L = \left(\frac{k_{\mathrm{B}}}{e}\right)^2\frac{(1+\lambda)(3+\lambda)\Gamma(1+\lambda)\Gamma(3+\lambda)\mathcal{F}_\lambda\mathcal{F}_{\lambda+2} - (2+\lambda)^2(\Gamma(2+\lambda))^2{\mathcal{F}_{\lambda+1}}^2}{(1+\lambda)^2(\Gamma(1+\lambda))^2{\mathcal{F}_\lambda}^2}. \quad (17)$$

As it only depends on the reduced Fermi level, its relative *SD*, sd_L, is given by

$$sd_L{}^2 = \left(\frac{SD_\alpha}{L}\right)^2 \left(\frac{\partial \eta}{\partial \alpha}\right)^2 \left(\frac{\partial L}{\partial \eta}\right)^2. \tag{18}$$

6. The electronic thermal conductivity is calculated using the electrical conductivity and Lorenz number as follows:

$$\kappa_\mathrm{E} = L\sigma T. \tag{19}$$

Its relative SD, sd_{κ_E}, is written as

$$sd_{\kappa_\mathrm{E}}{}^2 = sd_\sigma{}^2 + sd_L{}^2. \tag{20}$$

7. Electronic thermal conductivity is commonly used to determine κ_L using the relation, $\kappa_\mathrm{L} = \kappa - \kappa_\mathrm{E}$; sd_{κ_L} is then given by

$$sd_{\kappa_\mathrm{L}}{}^2 = sd_\kappa{}^2 + sd_{\kappa_\mathrm{E}}{}^2. \tag{21}$$

8. Finally, the uncertainty in the β parameter can be calculated using

$$sd_\beta{}^2 = sd_{\mu_0}{}^2 + \left(\frac{3}{2} sd_{m_D^*}\right)^2 + sd_{\kappa_\mathrm{L}}{}^2. \tag{22}$$

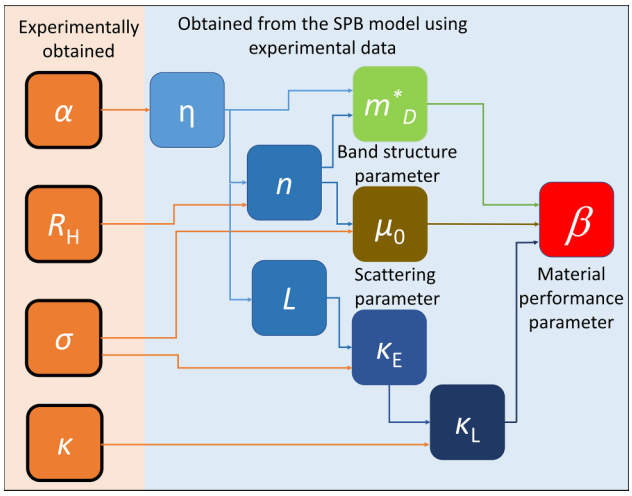

FIG. 1. A flowchart depicting the experimentally determined TE quantities, i.e., α, σ, and R_H (orange background) and the quantities obtained through the experimental data using the SPB model (blue background).

A flowchart summarizing the experimentally determined thermoelectric quantities and the associated SPB-derived quantities is given in Fig. 1. The expressions for the

TABLE I. Summary of the expressions for standard deviations in various SPB model-derived parameters due to SD in experimental data. Here, sd_i and SD_i denote relative and absolute standard deviations, respectively. Expressions for related derivatives are given in Table II.

SPB-derived quantity	Experimental quantity involved	Expression for standard deviation
Reduced Fermi level, η	α	$SD_\eta^2 = SD_\alpha^2 \left(\frac{\partial \eta}{\partial \alpha}\right)^2$
Carrier concentration, n	α, R_H	$sd_n{}^2 = sd_{R_H}{}^2 + \left(\frac{SD_\alpha}{r_H}\right)^2 \left(\frac{\partial r_H}{\partial \eta}\right)^2 \left(\frac{\partial \eta}{\partial \alpha}\right)^2$
Density of states mass, m_D^*	α, R_H	$sd_{m_D^*}{}^2 = \left(\frac{2}{3} sd_{R_\mathrm{H}}\right)^2 + \left(\frac{SD_\alpha}{J_{m_D^*}}\right)^2 \left(\frac{\partial J_{m_D^*}}{\partial \eta}\right)^2 \left(\frac{\partial \eta}{\partial \alpha}\right)^2$, $J_{m_D^*} = \left(\frac{(0.5+2\lambda)\Gamma(0.5+2\lambda)}{(1+\lambda)^2(\Gamma(1+\lambda))^2} \frac{\mathcal{F}_{2\lambda-0.5}}{\mathcal{F}_\lambda{}^2}\right)^{2/3}$
Mobility parameter, μ_0	α, σ, R_H	$sd_{\mu_0}{}^2 = sd_\sigma{}^2 + sd_{R_\mathrm{H}}{}^2 + \left(\frac{SD_\alpha}{J_{\mu_0}}\right)^2 \left(\frac{\partial J_{\mu_0}}{\partial \eta}\right)^2 \left(\frac{\partial \eta}{\partial \alpha}\right)^2$, $J_{\mu_0} = \frac{(1+\lambda)\Gamma(1+\lambda)}{(0.5+2\lambda)\Gamma(0.5+2\lambda)} \frac{\mathcal{F}_\lambda}{\mathcal{F}_{2\lambda-0.5}}$
Deformation potential, E_def	α, σ, R_H	$sd_{E_{def}}{}^2 = \left(\frac{1}{2} sd_{\mu_0}\right)^2 + \left(\frac{5}{4} sd_{m^*{}_D}\right)^2$
Lorenz number, L	α	$sd_L{}^2 = \left(\frac{SD_\alpha}{L}\right)^2 \left(\frac{\partial L}{\partial \eta}\right)^2 \left(\frac{\partial \eta}{\partial \alpha}\right)^2$
Electronic thermal conductivity, κ_E	α, σ	$sd_{\kappa_E}{}^2 = sd_\sigma{}^2 + sd_L{}^2$
Lattice thermal conductivity, κ_L	α, σ, κ	$sd_{\kappa_L}{}^2 = sd_\kappa{}^2 + sd_{\kappa_E}{}^2$
β parameter	$\alpha, \sigma, \kappa, R_\mathrm{H}$	$sd_\beta^2 = sd_{\mu_0}{}^2 + \left(\frac{3}{2} sd_{m_D^*}\right)^2 + sd_{\kappa_L}{}^2$

TABLE II. Expressions for the derivatives of terms dependent on the reduced Fermi level, used in calculating standard deviations in the SPB parameters, as given in Table I.

Derivative	Expression in terms of Fermi-Dirac integrals
$\frac{\partial \eta}{\partial \alpha}$	$\frac{1}{\partial \alpha/\partial \eta}; \frac{\partial \alpha}{\partial \eta} = \left(\frac{e}{k_B}\right)\left(K_\eta \frac{\mathcal{F}_\lambda^2 - \mathcal{F}_{\lambda-1}\mathcal{F}_{\lambda+1}}{\mathcal{F}_\lambda^2} - 1\right); K_\eta = \frac{(2+\lambda)\Gamma(\lambda+2)}{(1+\lambda)\Gamma(\lambda+1)}$
$\frac{\partial r_H}{\partial \eta}$	$K_{r_H}\left(\frac{\mathcal{F}_{2\lambda-1.5}\mathcal{F}_{0.5}\mathcal{F}_\lambda^2 + \mathcal{F}_{2\lambda-0.5}\mathcal{F}_{-0.5}\mathcal{F}_\lambda^2 - 2\mathcal{F}_\lambda\mathcal{F}_{\lambda-1}\mathcal{F}_{2\lambda-0.5}\mathcal{F}_{0.5}}{\mathcal{F}_\lambda^4}\right)$
	$K_{r_H} = \frac{3\sqrt{\pi}}{4}\frac{(0.5+2\lambda)\Gamma(0.5+2\lambda)}{(1+\lambda)^2(\Gamma(1+\lambda))^2}$
$\frac{\partial J_{m_D^*}}{\partial \eta}$	$\frac{2}{3}K_{J_{m_D^*}}\left(\frac{\mathcal{F}_{2\lambda-0.5}}{\mathcal{F}_\lambda{}^2}\right)^{-1/3}\left(\frac{\mathcal{F}_{2\lambda-1.5}\mathcal{F}_\lambda^2 - 2\mathcal{F}_\lambda\mathcal{F}_{\lambda-1}\mathcal{F}_{2\lambda-0.5}}{\mathcal{F}_\lambda^4}\right)$
	$K_{J_{m_D^*}} = \left(\frac{(0.5+2\lambda)\Gamma(0.5+2\lambda)}{(1+\lambda)^2(\Gamma(1+\lambda))^2}\right)^{2/3}$
$\frac{\partial J_{\mu_0}}{\partial \eta}$	$K_{J_{\mu_0}}\frac{\mathcal{F}_{\lambda-1}\mathcal{F}_{2\lambda-0.5} - \mathcal{F}_{2\lambda-1.5}\mathcal{F}_\lambda}{\mathcal{F}_{2\lambda-0.5}{}^2}$
	$K_{J_{\mu_0}} = \frac{(1+\lambda)\Gamma(1+\lambda)}{(0.5+2\lambda)\Gamma(0.5+2\lambda)}$
$\frac{\partial L}{\partial \eta}$	$\left(\frac{k_B}{e}\right)^2 \frac{1}{K_{L3}\mathcal{F}_\lambda^4}(K_{L1}(\mathcal{F}_{\lambda-1}\mathcal{F}_{\lambda+2} + \mathcal{F}_{\lambda+1}\mathcal{F}_\lambda)\mathcal{F}_\lambda{}^2 - 2K_{L2}\mathcal{F}_{\lambda+1}\mathcal{F}_\lambda^3 - 2\mathcal{F}_\lambda\mathcal{F}_{\lambda-1}(K_{L1}\mathcal{F}_\lambda\mathcal{F}_{\lambda+2} - K_{L2}\mathcal{F}_{\lambda+1}{}^2)$
	$K_{L1} = (1+\lambda)(3+\lambda)\Gamma(1+\lambda)\Gamma(3+\lambda); K_{L2} = (2+\lambda)^2(\Gamma(2+\lambda))^2;$
	$K_{L3} = (1+\lambda)^2(\Gamma(1+\lambda))^2$

*SD*s in various SPB-derived quantities are summarized in Table I and related expressions for derivatives are given in Table II.

III. RESULTS

Acoustic phonon (AP) scattering ($\lambda = 0$) is the most commonly employed scattering mechanism within the SPB model, as it has been found to fit the experimental data quite effectively above room temperature [8]. As most known TE materials are polar, polar optical phonon (POP) scattering ($\lambda = 1$)is also a relevant scattering mechanism to consider [53,55,56]. Additionally, we have considered ionized impurity (II) scattering ($\lambda = 2$), which is relevant for doped materials, in particular at low temperatures, and neutral impurity (NI) scattering ($\lambda = 0.5$), which might be relevant at very low temperatures for lightly doped materials [53]. Since the dependence of the SPB-derived quantities on σ, R_H, and κ is straightforward, their dependence on only α needs to be analyzed further. The partial derivatives given in Table II indicate the SPB-derived quantities' sensitivity to changes in the Fermi level and, in turn, the Seebeck coefficient. These derivatives are plotted in Figs. 2(b)–2(f). The Fermi integrals $\mathcal{F}_j$ are integrated numerically for $j > -1$ and $\mathcal{F}_{-1.5}$ is evaluated using the relationship $\mathcal{F}_{-1.5} = d\mathcal{F}_{-0.5}/d\eta$. For $\mathcal{F}_{-1}$, the analytic expression $\mathcal{F}_{-1} = 1/1 + e^{-\eta}$ [54] is used. The Seebeck value for heavily doped materials, which is generally required for high zT, is typically <200 μV/K. From Fig. 2(b), it can be seen that the reduced Fermi level is most sensitive to the Seebeck coefficient value in this range. Thus, even a small uncertainty in α would lead to a large uncertainty in η. The difference between different scattering mechanisms is most pronounced in the sensitivity of the mobility parameter to η. This is not surprising as the calculated carrier mobility is likely to be most affected by the scattering mechanism. For NI scattering, the mobility parameter and the Hall prefactor are independent of η [Eqs. (6) and (15)] and, therefore, are not sensitive to it.

Sensitivity to η is only an intermediate factor in evaluating the uncertainty in SPB-derived quantities due to the relative *SD* in the Seebeck coefficient (denoted by $sd_{A,\alpha}$ where A is an SPB-derived parameter); $sd_{A,\alpha}$ can be evaluated using the expressions given in Table II, assuming $sd_\sigma{}^2 = sd_{R_H}{}^2 = 0$. For $sd_\alpha = 0.01$ (the plots can be easily scaled according to the actual value of sd_α), SD_η and $sd_{A,\alpha}$ are visualized in Fig. 3. Figure S1 in Supplemental Material [57] (including references [13,58,59]) shows the relative SD in η for $1 < \eta < 10$ for AP scattering. The standard deviation in the Fermi level at low values of the Seebeck coefficient (typical for heavily doped materials) is quite high and varies among different scattering mechanisms; η depends on the carrier concentration and doping level and is not an intrinsic feature of the band structure. Among other SPB-derived quantities, the DOS mass—an important quantity associated with the electronic band structure—is by far the most affected. Assuming $sd_\alpha = 5\%$ (based on round-robin tests' reports [39,40])

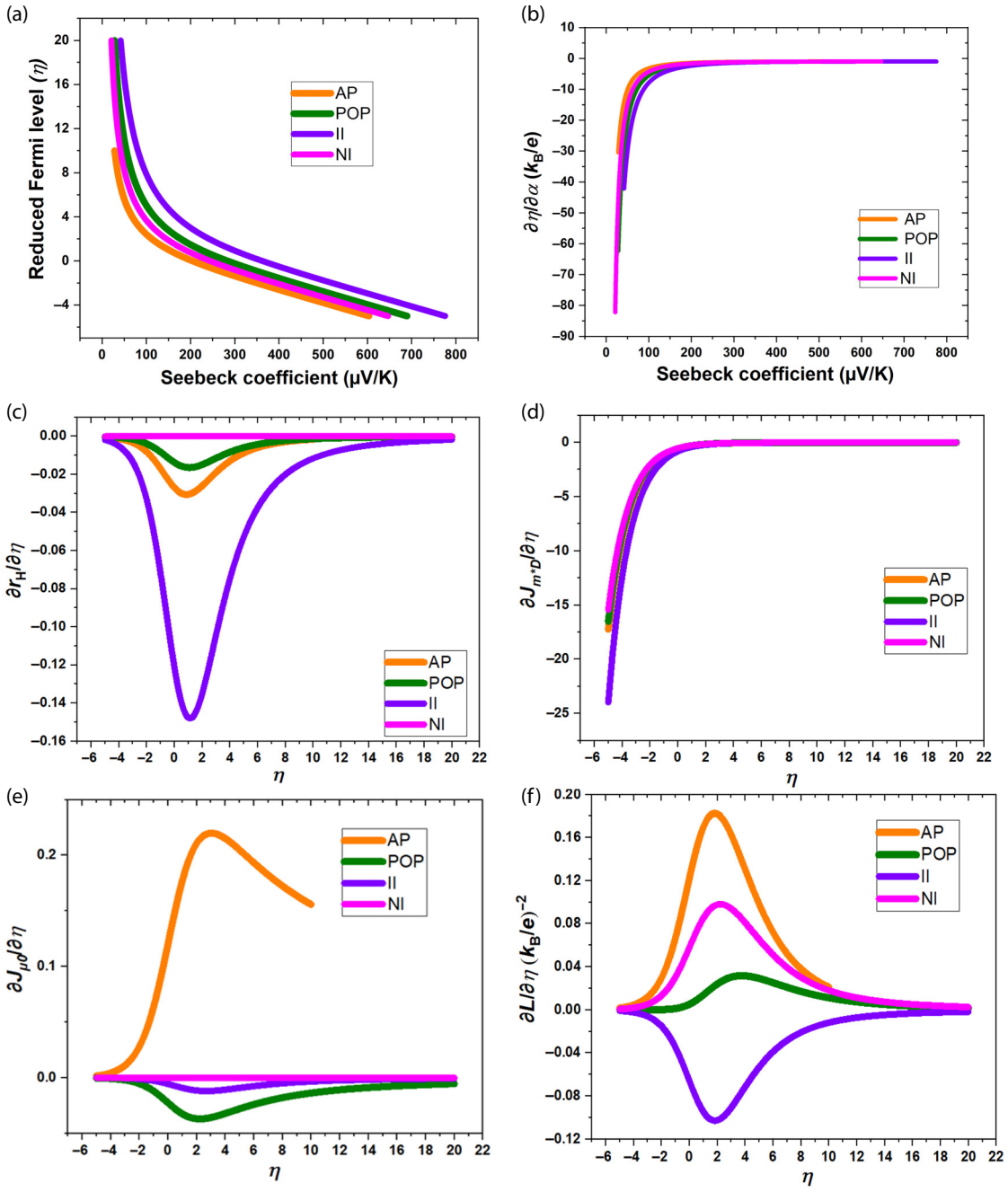

FIG. 2 (a) Seebeck coefficient as a function of the reduced Fermi level for different scattering mechanisms. (b) Sensitivity of the reduced Fermi level to the Seebeck coefficient. Sensitivity of the (c) Hall coefficient, (d) density of states effective mass, (e) mobility parameter and (f) Lorenz number to the reduced Fermi level (factors in the expressions of these SPB-derived quantities containing the reduced Fermi level are listed in Table I and the analytical expression for their derivatives plotted here are given in Table II). AP, POP, II, and NI denote the results assuming scattering with acoustic phonons, polar optical phonons, ionized impurities, and neutral impurities, respectively.

leads to $sd_{m_D^*,\alpha} = \sim 8.5\%$ at 200 μV/K for all scattering mechanisms considered. To estimate $sd_{m_D^*,\alpha}$ directly from the Seebeck coefficient, second-order polynomial fitting was employed for AP scattering as shown in Fig. 3(c). As $sd_{m_D^*,\alpha}$ for all considered scattering mechanisms are very similar in the fitting range, the same polynomial function can also be used to estimate $sd_{m_D^*,\alpha}$ for other scattering mechanisms. For all scattering mechanisms considered here, $sd_{m_D^*,\alpha}$ can be evaluated with a maximum deviation of 7% between 40 μV/K and 600 μV/K using (with α

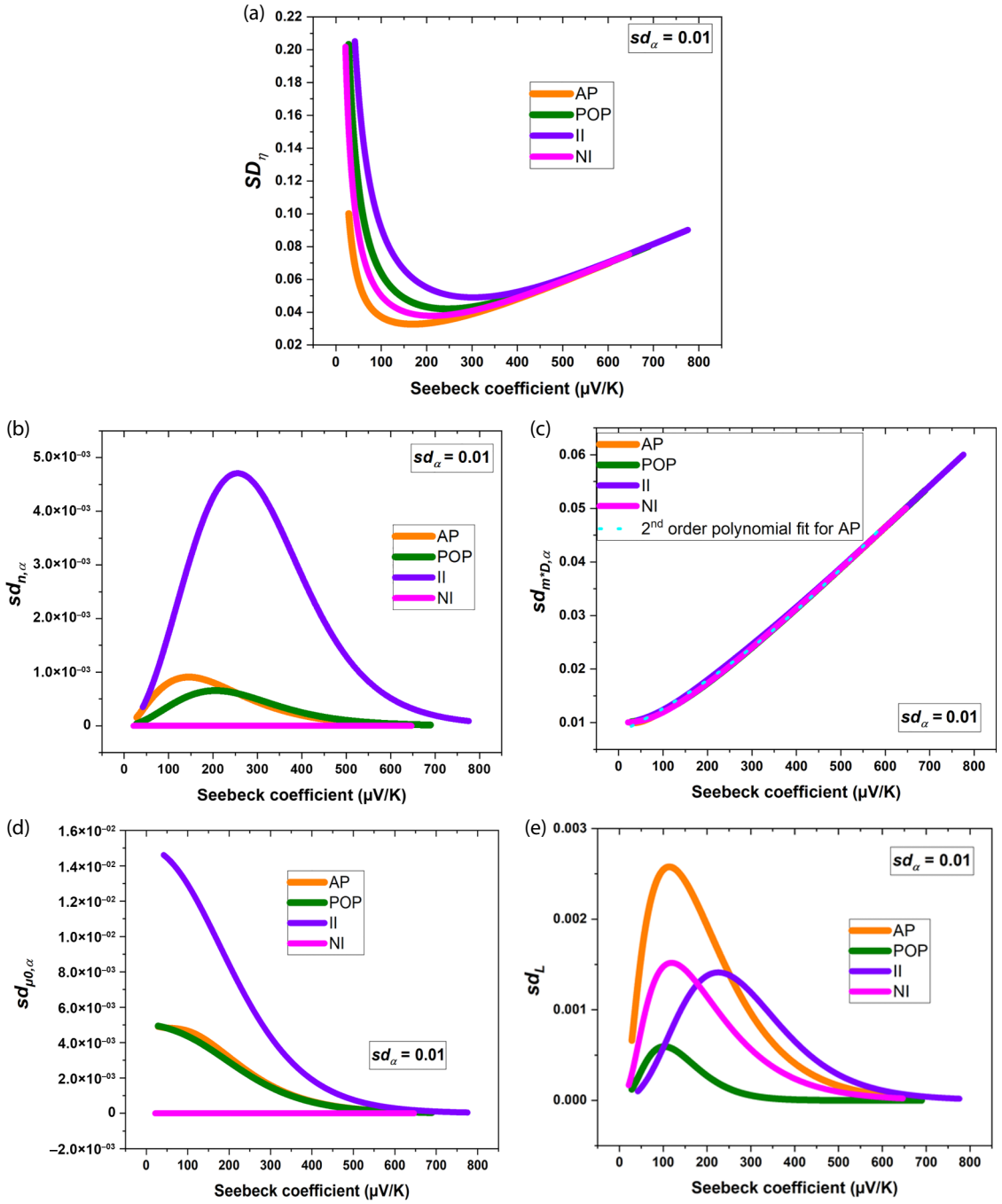

FIG. 3 (a)–(e) Standard deviations in the SPB-derived quantities only due to a standard deviation of 1% in the Seebeck coefficient. Here, *sd* and *SD* denote relative and absolute standard deviations, respectively.

in μV/K)

$$sd_{m^*_{D,\alpha}}(\alpha, sd_\alpha) = \mathrm{sd}_\alpha(\mathrm{b}_0 + \mathrm{b}_1\alpha + \mathrm{b}_2\alpha^2), \qquad (23)$$

where $b_0 = 8.115 \times 10^{-1}$, $b_1 = 4.113 \times 10^{-3}$ $(\mu\mathrm{V/K})^{-1}$, and $b_2 = 4.019 \times 10^{-6}$ $(\mu\mathrm{V/K})^{-2}$.

Similarly, curve fitting for $SD_{\eta,\alpha}$ and $sd_{\mu 0,\alpha}$ for AP scattering was employed and is shown in Fig. S2 with the associated functions and parameters given in Table S1 of the Supplemental Material [57]. The accuracy of these fits in the form of residuals is shown in Fig. S3 in the Supplemental Material [57]. The peak value of sd_L for AP scattering is the highest among all the mechanisms considered, at a maximum of ∼1.5% for $\mathrm{sd}_\alpha = 5\%$. Thus, sd_L can generally be ignored if sd_α is small. The highest values of $\mathrm{sd}_{n,\alpha}$ and $\mathrm{sd}_{\mu_0,\alpha}$ are observed for II scattering. For $\mathrm{sd}_\alpha = 5\%$, $\mathrm{sd}_{n,\alpha}$ would have the maximum value of ∼2.5% at ∼250 μV/K and $sd_{\mu_0,\alpha}$ would have a maximum value

of ∼7% at ∼40 μV/K. While ignoring $sd_{n,\alpha}$ might not cause any significant deficiencies in any modeling analysis, $sd_{\mu_{0},\alpha}$ can generally not be ignored. However, for AP and POP scattering, $sd_{\mu_{0},\alpha}$ remains small and, by assuming the measurement uncertainty in the electrical conductivity to be 5%, Eq. 14 gives the maximum total uncertainty in μ_0 as ∼5.6%. Thus, for these two mechanisms, the uncertainty in μ_0 caused by sd_α is small if sd_σ is comparable with or higher than sd_α, which is typically reported.

We have shown the uncertainties assuming a few commonly employed scattering mechanisms. The effect of different values of the scattering exponent can be observed for a general λ by evaluating the standard deviations at fixed values of the reduced Fermi level. This is plotted in Fig. S4 in the Supplemental Material [57]. Here, $sd_{n,\alpha}$ and $sd_{m^*_{D},\alpha}$ increase monotonously with λ while changes in $sd_{\mu_{0},\alpha}$ and sd_L are not monotonous for chosen values of η. For low values of sd_α, sd_L can still be ignored.

In Fig. 4, we plot the relative uncertainties in the SPB-derived parameters for AP scattering as a function of the Seebeck coefficient values, assuming $sd_\alpha = sd_\sigma = sd_\kappa =$ 5% and $sd_{R_H} = 10\%$. Uncertainties in n, μ_0, κ_E, and κ_L remain largely unaffected by the Seebeck coefficient values at ∼10%, ∼12%, ∼5%, and ∼7%, respectively. For m^*_D, the uncertainty increases strongly with increasing Seebeck coefficient and uncertainty between ∼8% and ∼17% for 50–400 μV/K (typical range for most of the good TE materials) can be expected. For the same range of Seebeck coefficients, the uncertainty in E_{def} amounts to between ∼12% and ∼20% and, in the β parameter, is between ∼18% and ∼30%.

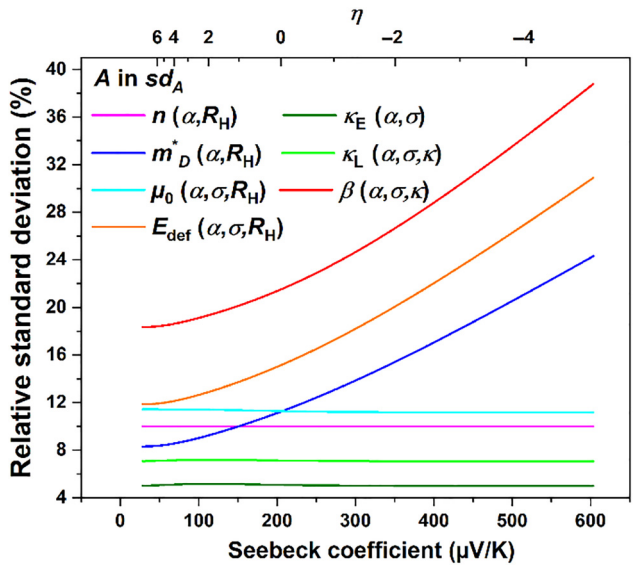

FIG. 4. Uncertainties in SPB-derived quantities for 5%, 5%, 5%, and 10% of uncertainty in α, σ, κ, and R_H, respectively.

IV. DISCUSSION

The uncertainty in the DOS mass obtained from the SPB model has many implications. Firstly, while comparing literature values for the DOS mass, one should account for the associated uncertainty based on Fig. 4. Secondly, it should be noted that the uncertainty in m^*_D is higher for higher values of the Seebeck coefficient. A higher Seebeck value is associated with the measurements of samples with large band gaps, with low doping or measurements at high temperatures. Materials with large band gaps or low doping are often poor TE materials and of less practical significance. However, often materials are synthesized with varying carrier concentrations in order to optimize material properties. If the doping concentration is varied for a material for which the SPB assumption is valid, the resulting room temperature Seebeck coefficients will differ, with the lower-doped material having a higher Seebeck coefficient. Given that the uncertainty in m^*_D for a higher Seebeck coefficient is higher [Fig. 3(c)], the m^*_D value for this sample could be quite different than the one for the sample with higher doping (or lower Seebeck coefficient). This difference could be misconstrued as a manifestation of an erroneous SPB assumption and attributed, for instance, to the influence of the minority carrier band. The Seebeck coefficient also increases with temperature for most highly doped TE materials and so does the experimental uncertainty [35]. Thus, at high temperatures, $sd_{m^*_D}$ is higher due to an increased Seebeck coefficient and enlarged experimental uncertainty compared with the room temperature. In this case, for a single sample, the uncertainty in m^*_D increases with temperature and any deviation from the SPB model, which one would expect to see at high temperatures, could lie within the error bars, making it difficult to comment on the nature of the electronic band structure. Additionally, an even higher uncertainty is observed for the deformation potential. As E_{def} is also more affected by sample-to-sample variations due to the impact of changes in the microstructure, its high uncertainty due to the uncertainty of the underlying measurement quantities makes its analysis and comparisons among literature values all the more challenging. As the β parameter is impacted by the uncertainties of all four measurement quantities, it possesses the highest uncertainty among all the SPB-derived quantities. Thus, the significant uncertainty in the β parameter must be considered when employing it to prioritize one material over the other.

So far, we have looked at uncertainty in measurements in terms of standard deviation. While it is more practically relevant, another aspect of measuring a physical quantity is error. Error is the difference between the measured and true value (principally unknown). Instances might occur where a measuring apparatus systematically under- or over-estimates a physical quantity. Martin [35], using a custom-built apparatus, demonstrated that a four-probe

measurement overestimates the Seebeck coefficient due to nonideal thermal contact between the sample and thermocouple. In this design, the cold finger effect (asymmetric parasitic heat flow from the sample to the environment) leads to an underestimation of the temperature difference and, thus, leads to an overestimation of α [42,60]. On the other hand, for the two-probe arrangement, poor thermal contact leads to an overestimation of the temperature difference and, hence, an underestimation of the Seebeck coefficient. Microprobe measurement techniques also usually underestimate the Seebeck coefficient [61,62]. Finite-sized contacts in the van der Pauw configuration lead to systematic under- or over-estimation of the Hall coefficient and electrical conductivity, depending on the ratio of material and contact resistivity, and it can be challenging to calculate the corresponding correction factors [63,64]. Thermal conductivity and zT measurements also have systematic errors due to radiation loss to the environment at high temperatures, leading typically to an overestimation of κ and an underestimation of zT [65–67]. If an estimate of the amount of under- or over-estimation can be made, it is possible to correct for it. However, it is more common to know the direction of the error than its magnitude. Therefore, it is worthwhile to assess the impact of measurement error on the SPB-derived quantities. As m_D^* is least affected by microstructure or synthesis routes, making it easier to compare among samples, we discuss how it is affected by error in the measurement of α and R_H. Since $(\mathrm{d}\eta/\mathrm{d}\alpha) < 0$ [Fig. 2(b)], an overestimation of α leads to an underestimation of η. For $\mathrm{d}\eta < 0$, $dJ_{m_D^*}$ is positive [Fig. 2(d)], which implies that, for an overestimated α, m_D^* would be overestimated. If R_H is overestimated, n $(\propto (1/R_\mathrm{H}))$ is underestimated and so is, in turn, $m_D^* (\propto n^{2/3})$. Thus, there is a compensating effect of the overestimation in both α and R_H on m_D^*. Based on accurate, over-, and under-estimation of α and R_H, 9 (3^2) combinations of measurements are possible.

In Fig. 5(a), we use true values of 100 μV/K and 5×10^{-8} m^3/C at 300 K for α (with 5% error) and R_H (with 10% error), respectively, as an example, and plot m_D^* and n for those nine measurement combinations; AP scatter is assumed here but, as observed in Fig. 3, the calculation results for POP would be very similar. Using Eqs. (4), (6), (7), and (10), the true values of m_D^* and n are determined as 1.33×10^{26} m^{-3} and 1.32 m_e, respectively, while the other results are calculated using the same equations with the over- or underestimated values. It can be observed from Fig. 5(a) that the scatter in SPB-derived quantities, based on the specified example, can span across ∼±15% and ∼±10% for m_D^* and n, respectively. The standard deviation according to the equations in Table I (within which ∼68% of all the values lie for a normal distribution), is ∼±8% and ∼±10% for m_D^* and n [yellow rectangle in Fig. 5(a)], respectively. Usually, the offset in measurement is unknown and it is not possible to correct for errors, but this could be an additional source of scatter in data while comparing measurement results from different laboratories. Even while comparing data within one lab and for the same material, systematic errors in the measured properties can show up as a systematic change in the SPB-derived quantities. In Fig. 5(b), we plot the variation of the SPB-derived m_D^* with n for a 5% overestimation of α

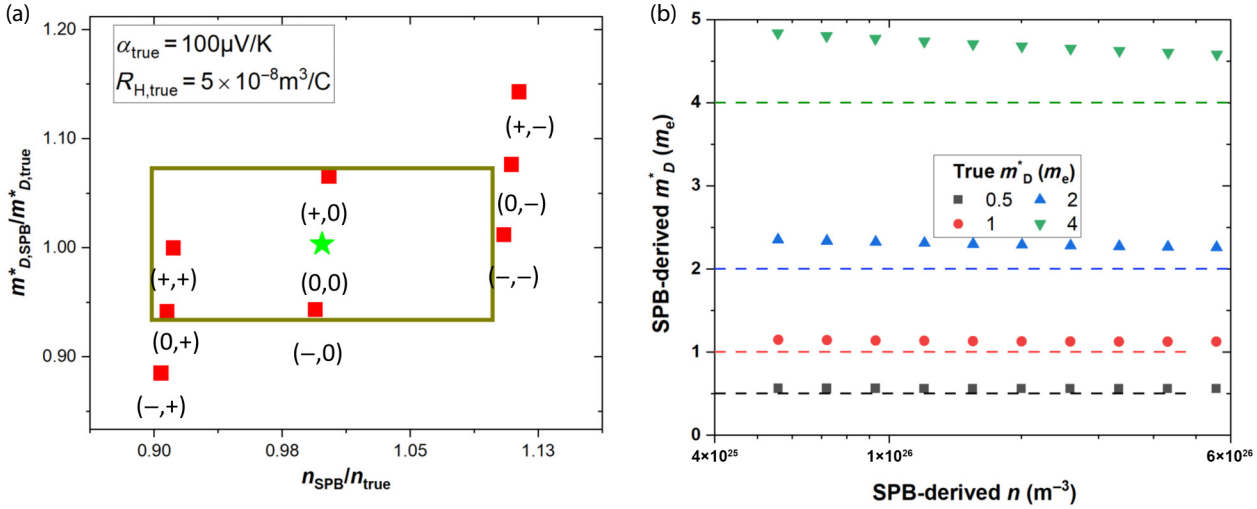

FIG. 5. (a) SPB-derived m_D^* and n from the Seebeck and Hall coefficients for nine combinations of ±5% and ±10% errors, respectively. First and second place in the brackets indicate error directions of the Seebeck and Hall coefficients, respectively, with 0, +, and − indicating accurate, overestimated, and underestimated quantities, respectively. The dark yellow rectangle indicates the span of one standard deviation from the true values of m_D^* and n, as calculated from the equations in Table I. (b) SPB-derived m_D^* vs n for four hypothetical SPB materials calculated assuming 5% overestimation of α and 10% underestimation in R_H. The dashed lines represent the true values of m_D^* for each case.

and a 10% underestimation in R_{H}, as it corresponds to the scenario which would result in maximum error in m_D^*. Four true values of m_D^* ranging from $0.5m_{\mathrm{e}}$ to $4m_{\mathrm{e}}$ (which would physically correspond to four different material compositions following the SPB model) are chosen. For each case, the m_D^* vs n plots could be misinterpreted to conclude that the SPB assumption is invalid when, in fact, the systematic variation of m_D^* with n is simply a manifestation of the systematic errors in α and R_H. It is also observed that the relative error escalates with increasing m_D^*, as for the plotted range of n, it varies from 13.2% to 12.6% for m_D^*=0.5 and from 20.9% to 14.5% for m_D^*=4. This provides further motivation to improve the measurement techniques as well as poses a significant challenge for obtaining reliable microscopic parameters using experimental data.

As m_D^* is the most cited band structure parameter, which is extracted using SPB modeling, it is common to compare literature values and almost equally common to find discrepancies in those values. In Fig. 6, assuming only AP scattering, we compare room temperature (RT) or near RT values for m_D^*, calculated using Seebeck and Hall coefficients in a temperature range between ∼300 and ∼380 K, collected from various literature sources [62,68–85] (including data available on Starrydata2 [86]). The samples had a nominal composition of $Mg_{2+\delta}Si_{1-x}A_x$, where $0 < \delta < 0.12$ and A denotes dopants (most of the samples were either Bi or Sb doped) with $x \leq 0.07$. A large

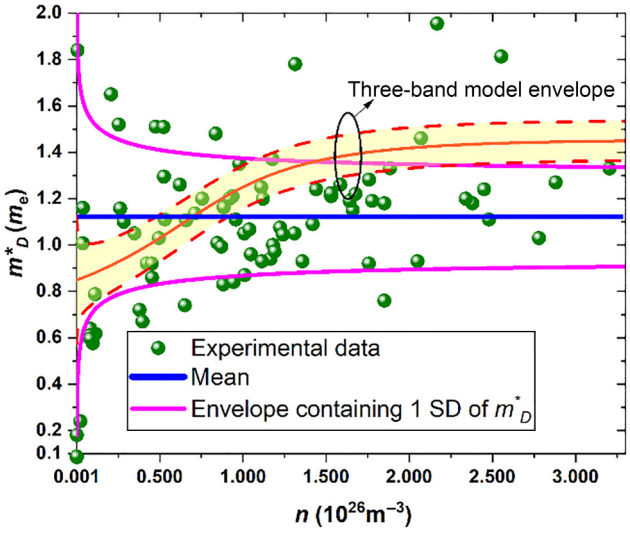

FIG. 6. Effective mass, m_D^*, for Mg_2Si, plotted as a function of the carrier concentration. Here, m_D^* is calculated using the SPB equations from α and R_H values at or near room temperature from various literature sources and the pink lines indicate the envelope of the mean effective mass ± the standard deviation assuming $sd_{R_H} = sd_\alpha = 15.7\%$. An SPB effective mass obtained from calculated transport properties using a three-band model of Mg_2Si [89] is also plotted along with an uncertainty envelope assuming 5% and 10% uncertainty in α and R_H, respectively.

scatter ($sd_{m_D^*} = 41\%$, assuming normal distribution) in m_D^* is observed, far from a constant value one would expect from a material that follows the SPB model. There could be various reasons for the scatter. For instance, grain boundaries with different properties than the bulk might influence the overall measured "composite" properties [87,88]. As grain size varies among preparation routes and samples, differences in grain sizes could have some systematic effect on α and R_{H} values leading to differing values of m_D^*. However, upon segregating the data according to different parameters such as grain size, material density, Mg content, and dopant species, wherever the information was directly available (Fig. S5 in the Supplemental Material [57]), we found no clear evidence that these attributes could resolve the observed scatter. Next, we calculated the amount of overall experimental scatter in α and R_{H}, which would lead to the observed scatter in m_D^*. We calculated the mean of the all the m_D^* values (which equates to 1.12 m_e) and assumed it to be the single true value of m_D^* for all the data shown. Using this true m_D^* value, we calculated the theoretical α for each n value plotted on the graph. Assuming equal uncertainty in α and R_{H}, and using

$$sd_{m_D^*}{}^2 = \left(\frac{2}{3} sd_{R_H}\right)^2 + (sd_{m_D^*,\alpha})^2$$

[with the empirical fit for $sd_{m_D^*,\alpha}$ given in Eq. (23)] for each value of the theoretically calculated α, we calculated the standard deviation for α and R_{H}, which would produce an envelope that contains ∼68% or one standard deviation of all the m_D^* values. This gave 16.4% of sd_{R_H} and sd_α each and is also shown in Fig. 6. A similar analysis was also performed on $CuGaTe_2$, which is also usually modeled with a single parabolic band [59] and, coincidentally, the scatter in the SPB mass could again be explained by a high uncertainty of 19% in $sd_{R_{\mathrm{H}}}$ and $sd_{m_D^*,\alpha}$ (Fig. S6 in the Supplemental Material [57]).

While this uncertainty is plausible for R_{H} at the first glance, this is a fairly high uncertainty for α, especially considering that the uncertainty in α from round-robin tests has been reported to be around 5% [38–40]. Due to the availability of limited literature data, this estimated standard deviation likely provides an upper limit on experimental uncertainty; the actual experimental uncertainty could still be lower but probably is not as low as is often reported. It is possible that round-robin tests reflect the most careful measurement conditions with the best samples and, practically, the measurement conditions and samples used in "standard measurements" are not chosen as carefully. It should also be noted that values for m_D^* have not been calculated in all the publications and, thus, unexpected differences between comparable samples might not have been identified at the time of the measurement. Systematic errors varying among instruments could also be a contributing factor in this large uncertainty.

Furthermore, we have assumed equal uncertainties for α and R_H here, while, e.g., a slightly larger uncertainty in R_H would lead to a reduced uncertainty in α required to explain the observed scatter. Finally, the calculations are performed assuming that Mg_2Si can be described by an SPB model. Non-SPB features might be masked by the scatter, in which case it is not the DOS mass that is being calculated but the SPB effective mass [90] for which this calculation of experimental uncertainty is not applicable. The exact band structure parameters for Mg_2Si are disputed and there is no generally accepted parameter set, with uncertainty in particular with respect to the energetic difference between the two lowest lying conduction bands. Recently, Agrawal *et al.* [89] fitted a 1VB + 2CB model to experimental data of a few differently doped samples and obtained a lower energetic difference between the two conduction bands than assumed earlier. Using their band structure model (parameters are listed in Table 4 in [89]) as an estimate of the potential influence of a further conduction band, we generated the Seebeck and Hall coefficients. Carrier concentration and the SPB effective mass were then calculated using the SPB model and are plotted in Fig. 6. With uncertainties of 5% and 10% assigned to α and R_H, respectively, the envelope of uncertainty (dotted red) around this SPB effective mass is also shown in Fig. 6. Most of the experimental data lies far away from this envelope and the expected systematic increase of the effective mass with carrier concentration cannot be inferred from the data. Thus, even if there is potentially an influence of a second conduction band, the analysis shows that the (large) experimental uncertainty is at least partially responsible for the observed scatter of the data.

The results of the uncertainty analysis of SPB-derived quantities can also be qualitatively extended to more complex band structures, e.g., one valence band (VB) and one conduction band (CB) model (with parabolic bands). At high temperatures, the minority carrier effects cannot be ignored and evidence of mixed conduction can be seen clearly in the transport properties of the material. For example, the Seebeck coefficient starts to decrease according to the following equation [13]:

$$\alpha = \frac{\alpha_{CB}\sigma_{CB} + \alpha_{VB}\sigma_{VB}}{\sigma_{CB} + \sigma_{VB}}. \tag{24}$$

Here, the subscripts denote the contributions from the two bands. As the two contributing Seebeck coefficients have opposite signs, this leads to a lower net α at high temperatures. Mixed conduction is of practical relevance as, generally, the maximum zT is attained at temperatures directly below the temperatures at which mixed conduction can be observed in the transport coefficients. As transport properties can be expressed as functions of the respective values of the individual bands, it is therefore plausible that the parameters extracted from more complex models depend on the uncertainties of the underlying measurement quantities at least as sensitively as for the SPB case. A key difference between single carrier transport and mixed conduction is the sensitivity of η on α and, for exemplary cases, we find that $d\eta/d\alpha$ is much larger in the mixed conduction regime (Fig. S7 in the Supplemental Material [57]). Even though further analysis is required to substantiate the point, this indicates that the provided estimates for the SPB-derived parameters represent a lower limit for the uncertainty in more complex cases.

V. CONCLUSION

In this work, we derive analytical expressions for the uncertainty of semiconductor parameters extracted from the SPB model based on uncertainty in measuring the thermoelectrical properties, i.e., Seebeck coefficient, α, electrical conductivity, σ, and Hall coefficient, R_H. While the uncertainty in SPB-derived quantities due to σ and R_H can be calculated in a straightforward manner, their dependence on the Seebeck coefficient is more complex and is, therefore, discussed in detail. Scattering by acoustic phonons, polar optical phonons, ionized impurities, and neutral impurities is considered. The uncertainty in most SPB-derived parameters also depends on the scattering mechanism. However, for the DOS mass, m_D^*, which is the most cited, relevant, and easy to compare parameter derived from the SPB model, the uncertainty does not change among different scattering mechanisms considered. A convenient fitting function is also provided to quickly estimate the uncertainty in m_D^* due to uncertainty in α, bypassing the need for evaluating Fermi integrals. As acoustic phonon scattering is most commonly employed as the dominant scattering mechanism, overall uncertainties are quantified and reported for it. Based on literature reports, we assume uncertainties in α, σ, κ, and R_H to be 5%, 5%, 5%, and 10%, respectively. For 5% uncertainty in α, the uncertainty in the Lorenz number can be ignored and the uncertainty in the carrier concentration, mobility parameter, and electronic thermal conductivity due to the uncertainty in α are quite small ($<0.5\%$, $<2.5\%$ and $<1.25\%$, respectively). The uncertainties in μ_0 and κ_E are $\sim$11% and $\sim$5%, respectively. The deformation potential has the highest uncertainty among all the SPB-derived quantities, varying from $\sim$12% to $\sim$20% between 50 μV/K and 400 μV/K. The uncertainty in the β parameter, which is often used as a criterion for selecting good TE materials, within the same range of Seebeck coefficients, is between $\sim$18% and $\sim$30%. We also show that systematic errors can lead to apparent changes in m_D^*, which could be misconstrued as manifestations of the electronic band structure. While comparing extracted literature values of m_D^* for Mg_2Si, we observe a large scatter in m_D^* (standard deviation of 41%), which could be explained by a $\sim$16% standard deviation in both α and R_H, indicating that only

the measurements performed under ideal conditions with ideal samples would lead to 5% uncertainty in the Seebeck coefficient, as reported for the round-robin measurements. Additionally, non-SPB features can become masked by the large uncertainty in the calculated m_D^*, preventing us from drawing meaningful conclusions about the features of the electronic band structure. Thus, this work provides an additional tool to analyze SPB calculations and further motivation to improve measurement protocols.

ACKNOWLEDGMENTS

H.N. would like to thank the German Academic Exchange Service (DAAD) for financial support.

The authors declare no conflict of interest.

DATA AVAILABILITY

The data that support the findings of this article are openly available [91].

[1] C. Candolfi, S. El Oualid, D. Ibrahim, S. Misra, O. El Hamouli, A. Léon, A. Dauscher, P. Masschelein, P. Gall, P. Gougeon, *et al.*, Thermoelectric materials for space applications, CEAS Space J. **13**, 325 (2021).

[2] D. Beretta, N. Neophytou, J. M. Hodges, M. G. Kanatzidis, D. Narducci, M. Martin-Gonzalez, M. Beekman, B. Balke, G. Cerretti, W. Tremel, *et al*, Thermoelectrics: From history, a window to the future, Mater. Sci. Eng., R **138**, 100501 (2019).

[3] S. Sharma, V. K. Dwivedi, and S. N. Pandit, A review of thermoelectric devices for cooling applications, Int. J. Green Energy **11**, 899 (2014).

[4] L. E. Bell, Cooling, heating, generating power, and recovering waste heat with thermoelectric systems, Science **321**, 1457 (2008).

[5] G. Tan, L.-D. Zhao, and M. G. Kanatzidis, Rationally designing high-performance bulk thermoelectric materials, Chem. Rev. **116**, 12123 (2016).

[6] X.-L. Shi, J. Zou, and Z.-G. Chen, Advanced thermoelectric design: from materials and structures to devices, Chem. Rev. **120**, 7399 (2020).

[7] Ning Jia, Jing Cao, Xian Yi Tan, Jinfeng Dong, Hongfei Liu, Chee Kiang Ivan Tan, Jianwei Xu, Qingyu Yan, Xian Jun Loh, and Ady Suwardi, Thermoelectric materials and transport physics, Mater. Today Phys. **21**, 100519 (2021).

[8] A. F. May and G. J. Snyder, in *Materials, Preparation, Characterization in Thermoelectrics*, edited by D. M. Rowe, 1st ed. (CRC Press, Boca Raton, 2012).

[9] W. Liu, H. Chi, H. Sun, Q. Zhang, K. Yin, X. Tang, Q. Zhang, and C. Uher, Advanced thermoelectrics governed by a single parabolic band: $Mg_2Si_{0.3}Sn_{0.7}$, a canonical example, Phys. Chem. Chem. Phys. **16**, 6893 (2014).

[10] M. Heo, S.-H. Kwon, S.-i. Kim, H. Park, K. H. Lee, and H.-S. Kim, Impact of resonant state formation and band convergence in In and Sr co-doped SnTe thermoelectric material evaluated via the single parabolic band model, J. Alloys Compd. **954**, 170144 (2023).

[11] H. Wang, A. D. LaLonde, Y. Pei, and G. J. Snyder, The criteria for beneficial disorder in thermoelectric solid solutions, Adv. Funct. Mater. **23**, 1586 (2013).

[12] M. Wood, U. Aydemir, S. Ohno, and G. J. Snyder, Observation of valence band crossing: the thermoelectric properties of $CaZn_2Sb_2$–$CaMg_2Sb_2$ solid solution, J. Mater. Chem. A **6**, 9437 (2018).

[13] H. Naithani, E. Müller, and J. de Boor, Developing a two-parabolic band model for thermoelectric transport modelling using Mg_2Sn as an example, J. Phys.: Energy **4**, 045002 (2022).

[14] B. Agrawal, Tarachand, J. de Boor, and T. Dasgupta, Dopant induced band convergence leading to high thermoelectric power factor in Mg_2Sn, Mater. Today Phys. **40**, 101293 (2024).

[15] X. H. Liu, T. J. Zhu, H. Wang, L. P. Hu, H. H. Xie, G. Y. Jiang, G. J. Snyder, and X. B. Zhao, Low electron scattering potentials in high performance $Mg_2Si_{0.45}Sn_{0.55}$ based thermoelectric solid solutions with band convergence, Adv. Energy Mater. **3**, 1238 (2013).

[16] W. Liu, X. J. Tan, K. Yin, H. J. Liu, X. F. Tang, J. Shi, Q. J. Zhang, and C. Uher, Convergence of conduction bands as a means of enhancing thermoelectric performance of n-type $Mg_2Si_{1-x}Sn_x$ solid solutions, Phys. Rev. Lett. **108**, 166601 (2012).

[17] P. Ying, L. Wilkens, H. Reith, N. P. Rodriguez, X. Hong, Q. Lu, C. Hess, K. Nielsch, and R. He, A robust thermoelectric module based on $MgAgSb/Mg_3(Sb, Bi)_2$ with a conversion efficiency of 8.5% and a maximum cooling of 72 K, Energy Environ. Sci. **15**, 2557 (2022).

[18] A. Duparchy, L. Millerand, J. Camut, S. Tumminello, H. Kamila, R. Deshpande, A. Cowley, E. Mueller, and J. de Boor, Establishing synthesis–composition–property relationships for enhanced and reproducible thermoelectric properties of MgAgSb, J. Mater. Chem. A **10**, 21716 (2022).

[19] J. Camut, E. Müller, and J. de Boor, Analyzing the performance of thermoelectric generators with inhomogeneous legs: Coupled material–device modelling for Mg_2X-based TEG prototypes, Energies **16**, 3666 (2023).

[20] A. Sankhla, H. Kamila, H. Naithani, E. Mueller, and J. de Boor, On the role of Mg content in $Mg_2(Si, Sn)$: Assessing its impact on electronic transport and estimating the phase width by in situ characterization and modelling, Mater. Today Phys. **21**, 100471 (2021).

[21] A. Sankhla, H. Kamila, K. Kelm, E. Mueller, and J. de Boor, Analyzing thermoelectric transport in n-type $Mg_2Si_{0.4}Sn_{0.6}$ and correlation with microstructural effects: An insight on the role of Mg, Acta Mater. **199**, 85 (2020).

[22] H. Kamila, G. K. Goyal, A. Sankhla, P. Ponnusamy, E. Mueller, T. Dasgupta, and J. de Boor, Systematic analysis of the interplay between synthesis route, microstructure, and thermoelectric performance in p-type $Mg_2Si_{0.2}Sn_{0.8}$, Mater. Today Phys. **9**, 100133 (2019).

[23] K. H. Lee, S.-i. Kim, H.-S. Kim, and S. W. Kim, Band convergence in thermoelectric materials: Theoretical background and consideration on Bi–Sb–Te alloys, ACS Appl. Energy Mater. **3**, 2214 (2020).

[24] J. Cai, R. Wang, S. Zhuang, F. Gao, M. Zhang, Z. Zhang, X. Tan, G. Liu, and J. Jiang, Giant band convergence and high thermoelectric performance in n-Type PbSe induced by spin-orbit coupling, Adv. Funct. Mater. **34**, 2311217 (2024).
[25] H. Park, S.-i. Kim, J.-Y. Kim, S.-M. Hwang, and H.-S. Kim, Estimation of temperature-dependent band parameters for bi-doped SnSe with high thermoelectric performance, Ceramics **6**, 504 (2023).
[26] X. Chen, D. Parker, and D. J. Singh, Importance of non-parabolic band effects in the thermoelectric properties of semiconductors, Sci. Rep. **3**, 3168 (2013).
[27] G. C. La Rocca and M. Cardona, Light-hole non-parabolicity in the single band approximation, Phys. Status Solidi B **167**, 115 (1991).
[28] J. Mao, W. Liu, and Z. Ren, Carrier distribution in multi-band materials and its effect on thermoelectric properties, J. Materiomics **2**, 203 (2016).
[29] Y. Kajikawa, Multi-band analysis of thermoelectric properties of n-type $Co_{1-x}Ni_xSb_3$ ($0 \leq x \leq 0.01$) over a wide temperature range of 10–773 K, J. Alloys Compd. **664**, 338 (2016).
[30] J. de Boor, On the applicability of the single parabolic band model to advanced thermoelectric materials with complex band structures, J. Materiomics **7**, 603 (2021).
[31] H. Wang, R. Gurunathan, C. Fu, R. Cui, T. Zhu, and G. J. Snyder, Thermoelectric transport effects beyond single parabolic band and acoustic phonon scattering, Mater. Adv. **3**, 734 (2022).
[32] P. Jood, J. P. Male, S. Anand, Y. Matsushita, Y. Takagiwa, M. G. Kanatzidis, G. J. Snyder, and M. Ohta, Na doping in PbTe: solubility, band convergence, phase boundary mapping, and thermoelectric properties, J. Am. Chem. Soc. **142**, 15464 (2020).
[33] T. Fang, X. Li, C. Hu, Q. Zhang, J. Yang, W. Zhang, X. Zhao, D. J. Singh, and T. Zhu, Complex band structures and lattice dynamics of Bi_2Te_3-based compounds and solid solutions, Adv. Funct. Mater. **29**, 1900677 (2019).
[34] C. Chang, G. Tan, J. He, M. G. Kanatzidis, and L.-D. Zhao, The thermoelectric properties of SnSe continue to surprise: extraordinary electron and phonon transport, Chem. Mater. **30**, 7355 (2018).
[35] J. Martin, Protocols for the high temperature measurement of the Seebeck coefficient in thermoelectric materials, Meas. Sci. Technol. **24**, 085601 (2013).
[36] Y. Liu, C. Fu, H. Xie, X. Zhao, and T. Zhu, Reliable measurements of the Seebeck coefficient on a commercial system, J. Mater. Res. **30**, 2670 (2015).
[37] J. de Boor, C. Stiewe, P. Ziolkowski, T. Dasgupta, G. Karpinski, E. Lenz, F. Edler, and E. Mueller, High-temperature measurement of Seebeck coefficient and electrical conductivity, J. Electron. Mater. **42**, 1711 (2013).
[38] Hsin Wang, Shengqiang Bai, Lidong Chen, Alexander Cuenat, Giri Joshi, Holger Kleinke, Jan König, Hee Woong Lee, Joshua Martin, Min-Wook Oh, *et al.*, International round-robin study of the thermoelectric transport properties of an n-Type half-Heusler compound from 300 to 773 K, J. Electron. Mater. **44**, 4482 (2015).
[39] P. Ziolkowski, C. Stiewe, J. de Boor, I. Druschke, K. Zabrocki, F. Edler, S. Haupt, J. König, and E. Mueller, Iron disilicide as high-temperature reference material for traceable measurements of Seebeck coefficient between 300 and 800 K, J. Electron. Mater. **46**, 51 (2017).
[40] H. Wang, Wallace D. Porter, Harold Bottner, Jan Konig, Lidong Chen, Shengqiang Bai, Terry M. Tritt, Alex Mayolett, J. Senawiratne, Charlene Smith, *et al.*, International round-robin testing of bulk thermoelectrics (Oak Ridge National Laboratory (ORNL), Oak Ridge, TN, 2011).
[41] T.-R. Wei, M. Guan, J. Yu, T. Zhu, L. Chen, and X. Shi, How to measure thermoelectric properties reliably, Joule **2**, 2183 (2018).
[42] J. Mackey, F. Dynys, and A. Sehirlioglu, Uncertainty analysis for common Seebeck and electrical resistivity measurement systems, Rev. Sci. Instrum. **85**, 085119 (2014).
[43] M. Schrade, T. Norby, and T. G. Finstad, Hall effect measurements on thermoelectric $Ca_3Co_4O_9$: On how to determine the charge carrier concentration in strongly correlated misfit cobaltites, J. Appl. Phys. **117**, 205103 (2015).
[44] M. Gunes, H. Sato, L. Pinsard-Gaudart, D. Berardan, and N. Dragoe, A versatile system for Hall effect measurements at high temperature, Meas. Sci. Technol. **28**, 105905 (2017).
[45] K. A. Borup, E. S. Toberer, L. D. Zoltan, G. Nakatsukasa, M. Errico, J.-P. Fleurial, B. B. Iversen, and G. J. Snyder, Measurement of the electrical resistivity and Hall coefficient at high temperatures, Rev. Sci. Instrum. **83**, 123902 (2012).
[46] A. Sankhala, 2024.
[47] Hsin Wang, Wallace D. Porter, Harald Böttner, Jan König, Lidong Chen, Shengqiang Bai, Terry M. Tritt, Alex Mayolet, Jayantha Senawiratne, Charlene Smith, *et al.*, Transport properties of bulk thermoelectrics: An international round-robin study, part II: Thermal diffusivity, specific heat, and thermal conductivity, J. Electron. Mater. **42**, 1073 (2013).
[48] H. Kamila, A. Sankhla, M. Yasseri, E. Mueller, and J. de Boor, Non-rigid band structure in Mg_2Ge for improved thermoelectric performance, Adv. Sci. **7**, 2000070 (2020).
[49] H. Naithani and T. Dasgupta, Critical analysis of single band modeling of thermoelectric materials, ACS Appl. Energy Mater. **3**, 2200 (2019).
[50] A. F. May, D. J. Singh, and G. J. Snyder, Influence of band structure on the large thermoelectric performance of lanthanum telluride, Phys. Rev. B **79**, 153101 (2009).
[51] C. M. Crawford, E. A. Bensen, H. A. Vinton, and E. S. Toberer, Efficacy of the method of four coefficients to determine charge-carrier scattering, Phys. Rev. Appl. **16**, 024004 (2021).
[52] H. H. Ku, Notes on the use of propagation of error formulas, J. Res. Natl. Bur. Stand. **70**, 263 (1966).
[53] V. I. Fistul, *Heavily Doped Semiconductors* (Plenum Press, New York, 1969), Vol. 1.
[54] J. Blakemore, Approximations for Fermi-Dirac integrals, especially the function F12 (η) used to describe electron density in a semiconductor, Solid-State Electron. **25**, 1067 (1982).
[55] J.-H. Bahk, Z. Bian, and A. Shakouri, Electron transport modeling and energy filtering for efficient thermoelectric $Mg_2Si_{1-x}Sn_x$ solid solutions, Phys. Rev. B **89**, 075204 (2014).

[56] C. J. Vineis, T. C. Harman, S. D. Calawa, M. P. Walsh, R. E. Reeder, R. Singh, and A. Shakouri, Carrier concentration and temperature dependence of the electronic transport properties of epitaxial PbTe and PbTe/PbSe nanodot superlattices, Phys. Rev. B **77**, 235202 (2008).

[57] See Supplemental Material at http://link.aps.org/supplemental/10.1103/lqtf-rvlm for additional fitting functions for a few SPB-derived parameters, further validation of the uncertainty analysis with experimental data, and an example to illustrate the relevance of uncertainty analysis beyond the single parabolic band model.

[58] G. J. Snyder, A. H. Snyder, M. Wood, R. Gurunathan, B. H. Snyder, and C. Niu, Weighted mobility, Adv. Mater. **32**, e2001537 (2020).

[59] J. Shen, Z. Chen, S. lin, L. Zheng, W. Li, and Y. Pei, Single parabolic band behavior of thermoelectric p-type $CuGaTe_2$, J. Mater. Chem. C **4**, 209 (2016).

[60] F. Edler and K. Huang, Analysis of the "cold finger effect" in measuring the Seebeck coefficient, Meas. Sci. Technol. **32**, 035014 (2020).

[61] P. Ziolkowski, M. Wambach, A. Ludwig, and E. Mueller, Application of high-throughput Seebeck microprobe measurements on thermoelectric half-Heusler thin film combinatorial material libraries, ACS Comb. Sci. **20**, 1 (2018).

[62] P. Ziolkowski, G. Karpinski, T. Dasgupta, and E. Müller, Probing thermopower on the microscale, Phys. Status Solidi A **210**, 89 (2013).

[63] R. Chwang, B. J. Smith, and C. R. Crowell, Contact size effects on the van der Pauw method for resistivity and Hall coefficient measurement, Solid-State Electron. **17**, 1217 (1974).

[64] J. Náhlík, I. Kašpárková, and P. Fitl, Influence of non-ideal circumferential contacts on errors in the measurements of the resistivity of layers using the van der Pauw method, Measurement **46**, 887 (2013).

[65] H. Kolb, T. Dasgupta, K. Zabrocki, E. Mueller, and J. de Boor, Simultaneous measurement of all thermoelectric properties of bulk materials in the temperature range 300–600 K, Rev. Sci. Instrum. **86**, 073901 (2015).

[66] J. de Boor and V. Schmidt, Complete characterization of thermoelectric materials by a combined van der Pauw approach, Adv. Mater. **22**, 4303 (2010).

[67] H. Naithani, P. Ziolkowski, and T. Dasgupta, Apparatus for measurement of thermoelectric properties of a single leg under large temperature differences, Rev. Sci. Instrum. **94**, 025104 (2023).

[68] J. De Boor, T. Dasgupta, H. Kolb, C. Compere, K. Kelm, and E. Mueller, Microstructural effects on thermoelectric efficiency: A case study on magnesium silicide, Acta Mater. **77**, 68 (2014).

[69] S. K. Bux, M. T. Yeung, E. S. Toberer, G. J. Snyder, R. B. Kaner, and J.-P. Fleurial, Mechanochemical synthesis and thermoelectric properties of high quality magnesium silicide, J. Mater. Chem. **21**, 12259 (2011).

[70] J. de Boor, C. Compere, T. Dasgupta, C. Stiewe, H. Kolb, A. Schmitz, and E. Mueller, Fabrication parameters for optimized thermoelectric Mg_2Si, J. Mater. Sci. **49**, 3196 (2014).

[71] Nader Farahi, Mathew VanZant, Jianbao Zhao, John S. Tse, Sagar Prabhudev, Gianluigi A. Botton, James R. Salvador, Ferenc Borondics, Zhenxian Liu, and Holger Kleinke, Sb-and Bi-doped Mg_2Si: location of the dopants, micro- and nanostructures, electronic structures and thermoelectric properties, Dalton Trans. **43**, 14983 (2014).

[72] M. Ioannou, G. Polymeris, E. Hatzikraniotis, K. Paraskevopoulos, and T. Kyratsi, Effect of Bi-doping and Mg-excess on the thermoelectric properties of Mg_2Si materials, J. Phys. Chem. Solids **75**, 984 (2014).

[73] M. Ioannou, G. Polymeris, E. Hatzikraniotis, A. Khan, K. Paraskevopoulos, and T. Kyratsi, Solid-state synthesis and thermoelectric properties of Sb-doped Mg_2Si materials, J. Electron. Mater. **42**, 1827 (2013).

[74] S. Chen, X. Zhang, W. Fan, T. Yi, D. V. Quach, S. Bux, Q. Meng, S. M. Kauzlarich, and Z. A. Munir, One-step low temperature reactive consolidation of high purity nanocrystalline Mg_2Si, J. Alloys Compd. **625**, 251 (2015).

[75] P. Nieroda, J. Leszczynski, and A. Kolezynski, Bismuth doped Mg_2Si with improved homogeneity: synthesis, characterization and optimization of thermoelectric properties, J. Phys. Chem. Solids **103**, 147 (2017).

[76] J.-i. Tani and H. Kido, Thermoelectric properties of Bi-doped Mg_2Si semiconductors, Phys. B **364**, 218 (2005).

[77] J.-i. Tani and H. Kido, Thermoelectric properties of Sb-doped Mg_2Si semiconductors, Intermetallics **15**, 1202 (2007).

[78] Effect of nanocomposite structure on the thermoelectric properties of 0.7-at% Bi-doped Mg_2Si nanocomposite, Chin. Phys. B **20**, 106202 (2011).

[79] J.-Y. Jung and I.-H. Kim, Solid-state synthesis of Te-doped Mg_2Si, J. Electron. Mater. **40**, 1144 (2011).

[80] J. Y. Jung, K. H. Park, and I. H. Kim, Thermoelectric properties of Sb-doped Mg_2Si prepared by solid-state synthesis, IOP Conf. Ser.: Mater. Sci. Eng. **18**, 142006 (2011).

[81] Kei Hayashi, Wataru Saito, Kazuya Sugimoto, Kenji Ohoyama, Kouichi Hayashi, Naohisa Happo, Masahide Harada, Kenichi Oikawa, Yasuhiro Inamura, and Yuzuru Miyazaki, Preparation, thermoelectric properties, and crystal structure of boron-doped Mg_2Si single crystals, AIP Adv. **10**, 035115 (2020).

[82] J. Zhao, Z. Liu, J. Reid, K. Takarabe, T. Iida, B. Wang, U. Yoshiya, and J. S. Tse, Thermoelectric and electrical transport properties of Mg_2Si multi-doped with Sb, Al and Zn, J. Mater. Chem. A **3**, 19774 (2015).

[83] K. Kambe and H. Udono, Convenient melt-growth method for thermoelectric Mg_2Si, J. Electron. Mater. **43**, 2212 (2014).

[84] Q. Zhang, X. Su, Y. Yan, H. Xie, T. Liang, Y. You, X. Tang, and C. Uher, Phase segregation and superior thermoelectric properties of $Mg_2Si_{1-x}Sb_x$ ($0 \leq x \leq 0.025$) prepared by ultrafast self-propagating high-temperature synthesis, ACS Appl. Mater. Interfaces **8**, 3268 (2016).

[85] D. A. Pshenai-Severin, M. I. Fedorov, and A. Y. Samunin, The influence of grain boundary scattering on thermoelectric properties of Mg_2Si and $Mg_2Si_{0.8}Sn_{0.2}$, J. Electron. Mater. **42**, 1707 (2013).

[86] Yukari Katsura, Masaya Kumagai, Takushi Kodani, Mitsunori Kaneshige, Yuki Ando, Sakiko Gunji, Yoji Imai, Hideyasu Ouchi, Kazuki Tobita, Kaoru Kimura, and Koji Tsuda, Data-driven analysis of electron relaxation times

in PbTe-type thermoelectric materials, Sci. Technol. Adv. Mater. **20**, 511 (2019).

[87] Yue Lin, Maxwell Wood, Kazuki Imasato, Jimmy Jiahong Kuo, David Lam, Anna N. Mortazavi, Tyler J. Slade, Stephen A. Hodge, Kai Xi, Mercouri G. Kanatzidis, *et al.*, Expression of interfacial Seebeck coefficient through grain boundary engineering with multi-layer graphene nanoplatelets, Energy Environ. Sci. **13**, 4114 (2020).

[88] J. J. Kuo, S. D. Kang, K. Imasato, H. Tamaki, S. Ohno, T. Kanno, and G. J. Snyder, Grain boundary dominated charge transport in Mg_3Sb_2-based compounds, Energy Environ. Sci. **11**, 429 (2018).

[89] B. Agrawal, J. de Boor, and T. Dasgupta, A multi-band refinement technique for analyzing electronic band structure of thermoelectric materials, Cell Rep. Phys. Sci. **5**, 101781 (2024).

[90] G. J. Snyder, A. Pereyra, and R. Gurunathan, Effective mass from Seebeck coefficient, Adv. Funct. Mater. **32**, 2112772 (2022).

[91] H. Naithani, doi:10.5281/zenodo.16419547 (Zenodo, 2025).